

Semantic-aware Dense Representation Learning for Remote Sensing Image Change Detection

Hao Chen, Wenyuan Li, Song Chen and Zhenwei Shi*, *Member, IEEE*

Abstract—Training deep learning-based change detection (CD) model heavily depends on labeled data. Contemporary transfer learning-based methods to alleviate the CD label insufficiency mainly upon ImageNet pre-training. A recent trend is using remote sensing (RS) data to obtain in-domain representations via supervised or self-supervised learning (SSL). Here, different from traditional supervised pre-training that learns the mapping from image to label, we leverage semantic supervision in a contrastive manner. There are typically multiple objects of interest (e.g., buildings) distributed in varying locations in RS images. We propose dense semantic-aware pre-training for RS image CD via sampling multiple class-balanced points. Instead of manipulating image-level representations that lack spatial information, we constrain pixel-level cross-view consistency and cross-semantic discrimination to learn spatially-sensitive features, thus benefiting downstream dense CD. Apart from learning illumination invariant features, we fulfill consistent foreground features insensitive to irrelevant background changes via a synthetic view using background swapping. We additionally achieve discriminative representations to distinguish foreground land-covers and other backgrounds. We collect large-scale image-mask pairs freely available in the RS community for pre-training. Extensive experiments on three CD datasets verify the effectiveness of our method. Ours significantly outperforms ImageNet, in-domain supervision, and several SSL methods. Empirical results indicate ours well alleviates data insufficiency in CD. Notably, we achieve competitive results using only 20% training data than random baseline using 100% data. Both quantitative and qualitative results demonstrate the generalization ability of our pre-trained model to downstream images even remaining domain gaps with the pre-training data. Our data and code will make public.

I. INTRODUCTION

REMOTE sensing (RS) image Change detection (CD) is the process of identifying changes of interest in the same geographical region by analyzing multi-temporal RS images captured at different times [1]. The definition of change varies across applications, such as urban expansion [2], agricultural surveys [3], deforestation monitoring [4], disaster damage assessment [5], etc.

The availability of multi-temporal very high-resolution (VHR) RS images from satellite data (e.g., WorldView-3,

QuickBird, and GaoFen-2) or aerial data, provides opportunities for monitoring land cover changes at a fine scale. CD based on VHR images still remains challenging due to two aspects: 1) the complexity of the object in a scene (i.e., objects of the same semantic meaning show different appearances with different geospatial locations and seasons), 2) diverse imaging conditions (e.g., sensor characteristics, viewing angles, and illumination conditions) [6]. A good CD model can identify real changes (e.g., buildings) while ignoring irrelevant changes (e.g., illumination, seasonal difference, and unconcerned land-cover changes).

Despite the great success of contemporary deep learning (DL)-based CD methods [7], the lack of a large labeled CD dataset limits their generalization to real-world applications. One effective solution to handle the data insufficiency is to fine-tune the model from ImageNet pre-training [8–13]. Considering the domain gap between natural and RS images may induce sub-optimal representations, a new trend is to pre-train on RS data to better learn the in-domain representations, including supervised pre-training [10, 14, 15] and self-supervised learning (SSL) [16–19]. Contrastive SSL [20, 21] could learn useful representations from massive unlabeled data by pulling together representations of semantically similar samples (i.e., positive pairs) and pushing away those of dissimilar samples (i.e., negative pairs). Very recently, contrastive methods have been introduced in the RS domain [16–18, 22–33] and have shown promising performance for the downstream supervised CD task [16–18].

Most existing contrastive methods in CD express each image view into one representation vector via uniform aggregation of pixel-level embeddings. Different from the object-centered natural image (e.g., ImageNet), there are typically multiple small objects (e.g., buildings) located in various positions in a real-world RS image. Contrastive learning on global representations that lack spatial information is not optimal for the downstream CD dense prediction task. Moreover, land cover spatial misalignment between different views (i.e., positive pairs) of the same image via artificial augmentations (e.g., random crop) may further hinder representation learning.

Based on the above observation, we propose a semantic-aware dense representation learning for remote sensing image CD. Instead of manipulating the global representations, we constrain the dense consistency of the pixel-level image embeddings according to the location correspondence in the overlapped area between the two views. Multiple spatial-aligned points between the two views are sampled to achieve dense correspondence. Our motivation is that the introduced point consistency may not only learn the high-level representations

This work was supported by the National Natural Science Foundation of China under Grant 62125102. (Corresponding author: Zhenwei Shi)

Hao Chen (email: justchenhao@buaa.edu.cn), Wenyuan Li (email: liwenyuan@buaa.edu.cn) and Zhenwei Shi (Corresponding Author, e-mail: shizhenwei@buaa.edu.cn) are with Image Processing Center, School of Astronautics, Beihang University, Beijing 100191, China, and with Beijing Key Laboratory of Digital Media, Beihang University, Beijing 100191, China, and also with State Key Laboratory of Virtual Reality Technology and Systems, School of Astronautics, Beihang University, Beijing 100191, China. Song Chen (email: justharrychen@naver.com) is with Department of Journalism and Communications, Jeonuk National University, Jeonju-si 54896, South Korea.

invariant to different augmentations (i.e., color and geometry transformations) but also sustain sensitivity to local spatial information, which helps the downstream dense prediction task. Towards semantic-aware representation learning, we obtain class-balanced sample points from each semantic region by leveraging the semantic mask. We follow SimSiam [21] to implement the cross-view (i.e., a positive pair) similarity between the sampled point pairs. Furthermore, we design an additional semantic dissimilar loss to guide the model to distinguish objects of interest (i.e., foreground) from other unconcerned land covers (i.e., background) via pushing away representations belonging to different semantics. Apart from learning features invariant to illumination changes, we further propose a virtual view via background synthesis to achieve consistent representations for the interest objects regardless of background changes. The synthetic view of the current image is generated by blending its foreground and the background from another image using the semantic mask.

We collect a pre-training dataset that contains large-scale RS images and corresponding building semantic masks. Notably, we leverage image-mask pairs that are freely available in RS society [34] to guide the contrastive pre-training. Our proposed method is evaluated on three public building change detection datasets [2, 35, 36]. Extensive experiments on the downstream CD task verify the effectiveness of the proposed pre-training method.

The contribution of our work can be summarised as followed:

- We propose semantic-aware pre-training based on dense class-balanced sampled points for RS image CD. Instead of manipulating image-level representations, we constrain pixel-level cross-view consistency as well as cross-semantic discrimination to learn spatially-sensitive features, thus benefiting the downstream dense prediction CD task.
- We leverage semantic supervision in a contrastive manner to enhance feature discrimination ability between objects of interest and background in the RS image. Apart from learning illumination invariant representations, we propose a virtual view via background synthesis to learn consistent foreground representations insensitive to irrelevant background changes.
- Extensive experiments on three CD datasets verify the effectiveness of the proposed method. Ours outperforms ImageNet pre-training, in-domain supervision, and several state-of-the-art SSL methods.

The rest of this paper is organized as follows. Sec. II introduces related work of CD data-efficiency approaches and pre-training methods. Sec. III describes the design of our proposed semantic-aware dense pre-training method. Experimental results are given in Sec. IV, and the Conclusion is drawn in Sec. V.

II. RELATED WORK

A. Handling label insufficiency in CD

Training DL-based models typically rely on a massive amount of labeled data. Despite a large amount of RS data,

high-quality labels via manual annotation could be costly. Many efforts in RS CD have been made to tackle the label insufficiency, including applying data augmentation [37–43], generating pseudo labels for unlabeled data via semi-supervised learning [36, 44, 45], using active learning to select a small number of informative samples [46–49], and fine-tuning a pre-trained model [8, 10, 16, 17, 19, 50, 51].

Data augmentation is an effective solution to enhance the size of the training dataset. The most common way is to use transformation-based augmentations [37, 39–43], including geometric transformations (e.g., random crop, horizontal flip), color transformations, and Gaussian blur, etc. A recent advance increases the number of the positive samples (change of interest) by blending the gan-generated instance on the appropriate spatial-temporal position of the bitemporal image [38].

Transfer a pre-trained model allows leveraging the knowledge of a source dataset to enhance the performance of a downstream task. ImageNet pre-training is widely used in change detection [7–13] and shows superior to random initialization, especially in small data regimes. Considering the domain gap between ImageNet and RS images, a new trend is to pre-train on the remote sensing data to learn the in-domain representations [10, 14–17, 19, 50–53]. Supervised pre-training on RS classification samples [10, 14, 15, 50, 51] is still limited by the amount of labeled data, while self-supervised pre-training could make use of the vast amount of unlabeled RS data [16, 17, 19].

Our method falls in the pre-training scope. Different from normal supervised pre-training methods that learn the mapping from image to label, we apply the semantic supervision in a contrastive manner to enhance the feature discrimination to different semantic categories in the SSL framework. Notably, we leverage image-mask pairs that are freely available in RS society to guide the contrastive pre-training.

Please note that a shorter, preliminary study of our semantic-aware representation learning has been presented in IGRASS 2022 [53]. This paper is a continuation and extension of our previous work by introducing two more pre-training designs related to the use of semantic information as well as supplementing more extensive experimental results, including more comparisons, ablations, and visualizations.

B. Contrastive pre-training methods

Self-supervised learning has attracted many researchers by virtue of its ability to learn good feature representations from massive unlabeled data to benefit various downstream tasks [54]. Currently, contrastive methods (e.g., SimCLR [55], MoCo [20, 56], BYOL [57], SimSiam [21] and DenseCL [58]) have made significant progress in SSL. The key of contrastive approaches is to perform the instance discrimination pretext task by pulling together representations of similar images (positive pairs) and pushing away those of dissimilar images (negative pairs). The InfoNCE loss [59] is typically applied to induce similarity between positive pairs and dissimilarity between negative pairs [11, 20, 55]. More recent attempts [21, 57] apply a simpler loss function (i.e., negative cosine

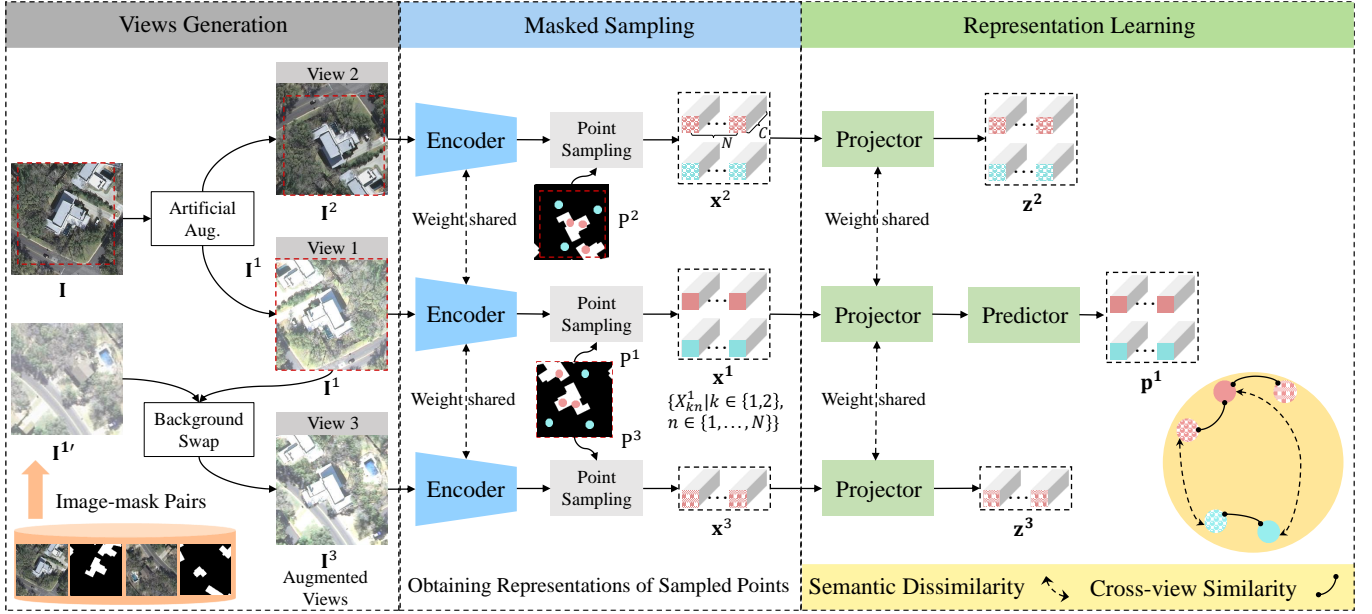


Fig. 1. Illustration of our semantic-aware dense representation learning. Our framework follows SimSiam [21] to use simple Siamese networks to learn meaningful image representations. Instead of constraining image-level consistency, we achieve point-level consistency across views to sustain spatially sensitive features, thus better transferring to the downstream dense prediction CD task. An equal number of points for each category are sampled from the overlapped region between views by leveraging the semantic mask. Apart from learning illumination invariant representations, we propose the background swap to learn consistent foreground representations regardless of background changes. We further use the semantic relation to learn discriminative features to distinguish between foreground and background.

similarity) that only relies on positive samples and does not use negative ones.

Very recently, many contrastive methods have been applied in RS to obtain in-domain pre-trained models that benefit downstream tasks, including land-cover classification [22, 24–28, 60, 61], semantic segmentation [29–32], and change detection [16–18]. Most existing methods apply InfoNCE loss [18, 22, 24–28, 30, 33, 62] or triple loss [17, 60] on the constructed positive and negative pairs. Positive samples can be obtained by different artificial augmentations (e.g., color and geometric transformations) of the same image [25, 28], spatial augmentations (i.e., geospatially overlapped images) [24, 27, 60], temporal augmentations (i.e., multi-temporal co-registered images) [16, 17, 22, 26, 62], and modality augmentations (e.g., optical image, SAR, and semantic mask) [29, 63]. Negative pairs can be different samples in a mini-batch or spatially distinct images [60, 62].

The contrastive methods for change detection have seldom been explored. Some attempts apply SSL directly on a small downstream change detection dataset to extract seasonally invariant features for unsupervised change detection [64–66]. Other more related studies that follow the normal SSL pipeline mostly evaluate the pre-trained model on the medium-resolution change detection dataset [16–18]. We instead explore pre-trained models suitable for high-resolution RS image change detection. Instead of applying the normal global consistency, we propose dense points consistency based on spatial correspondence between the positive pairs to better sustain the sensitivity of the spatial information, therefore benefiting the downstream dense prediction task, especially on VHR RS images that contain plenty of spatial details. Most existing

methods [16, 17, 64–66] treat co-registered multi-temporal images as positive samples to learn the seasonally invariant features. However, the intrinsic change of interest within the bitemporal image may induce the pre-trained model invariant to real changes, which may be unfavorable to the downstream CD task. Different from existing methods that force agreement between representations of bitemporal images, ours learns consistency of foreground representations between one image and its synthetic version whose background is replaced by that from another image. In this way, we leverage the virtual bitemporal images to guide the model pay more attention to interest foreground objects regardless of changes in unconcerned land covers.

III. SEMANTIC-AWARE DENSE REPRESENTATION LEARNING

In this section, we first give an overview of the proposed pre-training method for the downstream CD task and then introduce its three main components. Finally, implementation details are given.

A. Overview

To alleviate the insufficiency of labeled CD data, we explore a representation learning method by leveraging massively available data in the RS society. We collect large-scale image-mask pairs (see Sec. IV-A) in a painless manner for contrastive pre-training. Specially, we focus on the building category as the objects of interest to perform change detection.

We propose Semantic-aware Dense representation Learning (SaDL) for remote sensing image change detection. The goal

of SaDL is to learn a feature extractor that could 1) generate consistent representations invariant to illumination and color changes as well as changes of unconcerned land covers (i.e., background), 2) be able to distinguish objects of interest from the background, 3) sustain spatially sensitive features to reduce the gap with the downstream dense prediction CD task.

To achieve this, we introduce the semantic mask into a self-supervised learning framework. Fig. 1 illustrates the proposed SaDL. Following SimSiam [21], we use simple Siamese networks as the feature extractor to learn meaningful image representations without using negative samples. Our SaDL is composed of three main steps:

1) **Views Generation.** Apart from two views of the same image via normal augmentations (i.e., color and geometry transformation), we generate a third view by swapping its background with that from another image using the semantic mask. These views can be used to learn consistent representations invariant to illumination and background changes. More generation details are given in Sec. III-B.

2) **Masked Sampling.** Instead of obtaining image-level representations, our Siamese encoder converts each image view into dense per-pixel representations. We sample the same number of feature points from each semantic region in the overlapped area of the generated views. For more details see Sec. III-C.

3) **Representation Learning.** Given the sampled point representations, we employ MLP-based projection/prediction networks to perform feature transformations. We constrain the features by cross-view similarity and cross-semantic dissimilarity to learn representations that are invariant to irrelevant changes and discriminative to foreground/background. For more details see Sec. III-D.

B. Views Generation

Given each input training sample (including an image \mathbf{I} and a mask \mathbf{M}) in a mini-batch, we produce three views of the same image, including two normal-transformed versions, and one background-swapping version. Let $\mathcal{T} = \mathcal{T}_g \circ \mathcal{T}_c$ denotes a set of artificial augmentations, including color augmentations \mathcal{T}_c (e.g., color jetting and Gaussian blur) and geometric augmentations \mathcal{T}_g (e.g., random cropping and flipping). Details of our views generations are illustrated in Algorithm 1.

We first generate two views \mathbf{I}^i , $i \in \{1, 2\}$ of \mathbf{I} via different artificial augmentations:

$$\begin{aligned}\mathbf{I}^1 &= \mathcal{T}(\mathbf{I}) = \mathcal{T}_g(\mathcal{T}_c(\mathbf{I})) \\ \mathbf{I}^2 &= \mathcal{T}'(\mathbf{I}) = \mathcal{T}'_g(\mathcal{T}'_c(\mathbf{I}))\end{aligned}\quad (1)$$

where $\mathcal{T}, \mathcal{T}'$ denote two random sets of artificial augmentations.

The corresponding semantic masks \mathbf{M}^i for each view $i \in \{1, 2\}$ are also generated via applying the same geometric augmentation as that in the image:

$$\begin{aligned}\mathbf{M}^1 &= \mathcal{T}_g(\mathbf{M}) \\ \mathbf{M}^2 &= \mathcal{T}'_g(\mathbf{M}).\end{aligned}\quad (2)$$

Virtual view generation via background swapping. The third view of \mathbf{I} is obtained by swapping the background of

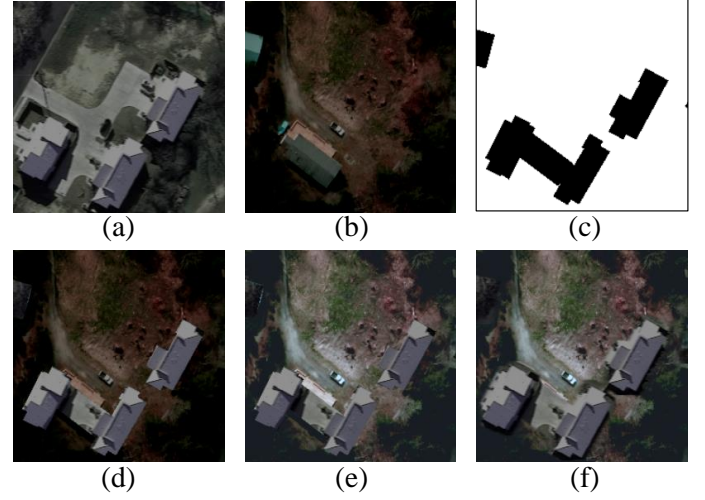


Fig. 2. Illustration of our view synthesis. View 3 is generated by swapping the background of (a) the view 1 of the current image \mathbf{I}^1 and that of (b) another image $\mathbf{I}^{1'}$ using (c) their common background mask \mathbf{M}_{bg} . We compare different compositions: (d) direct pasting, (e) with color transfer, (f) with color transfer + context-aware blending.

its first view \mathbf{I}^1 with that of another image $\mathbf{I}^{1'}$. For simplicity, $\mathbf{I}^{1'}$ has the inverted index as \mathbf{I} from the same mini-batch. In other words, the summation of the index of \mathbf{I} and that of $\mathbf{I}^{1'}$ equals the mini-batch size. Note that we only superimpose the background of $\mathbf{I}^{1'}$ but not its foreground, on the background of \mathbf{I}^1 because we aim to simulate the changes of unconcerned land covers. We obtain the common background mask \mathbf{M}_{bg} by calculating the intersection of the background regions in \mathbf{M}^1 and $\mathbf{M}^{1'}$.

However, directly pasting the background of $\mathbf{I}^{1'}$ on \mathbf{I}^1 using \mathbf{M}_{bg} may result in undesired synthetic artifacts (see Fig. 2 (d)) that could be detrimental to representation learning. Towards a realistic and effective image composite, we present a simple view synthesis method, including two main steps:

1) **Color transfer.** To reduce the domain gap between $\mathbf{I}^{1'}$ (source image) and \mathbf{I}^1 (target image), we employ a simple color transfer method [67] to change the color characteristic of one image to accord with another in the image domain. The key idea is to match the mean and variance of each channel of the transformed image to that of the target image. To be formal, the transformed image is given by

$$\mathbf{I}_t^{1'} = \sigma(\mathbf{I}^1) \left(\frac{\mathbf{I}^{1'} - \mu(\mathbf{I}^{1'})}{\sigma(\mathbf{I}^{1'})} \right) + \mu(\mathbf{I}^1) \quad (3)$$

where $\mu(\cdot), \sigma(\cdot)$ denote the means and variances computed across spatial dimensions independently for each channel of the image.

2) **Context-aware blending.** The mere presence of the context surrounding the foreground (e.g., building) is a critical cue for object recognition. For a realistic composite, we sustain the foreground area as well as its nearby context for image \mathbf{I}^1 by performing morphological erosion on the background mask. Moreover, we further blur the eroded background mask using a Gaussian filter towards natural and seamless composition. The

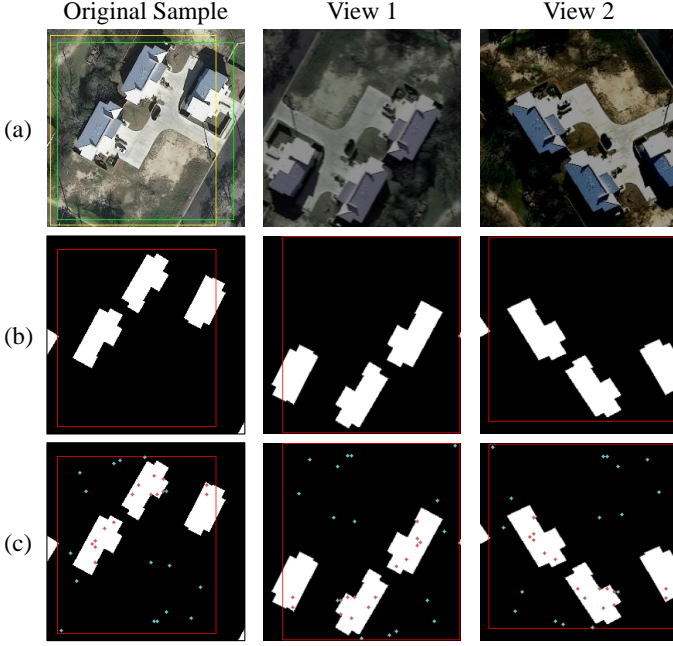


Fig. 3. Illustration of our masked sampling. (a) Images. View 1/2 corresponds to the region within the green/yellow bounding box in the original image. (b) Semantic masks. The overlapped region between views is shown in red. (c) Sampled points. The same number of points for each semantic region in the overlapped area are randomly sampled. Different colors are used for each category for better visualization.

composite image \mathbf{I}^3 (view 3) is calculated by alpha blending using the eroded mask of the blurred version:

$$\mathbf{I}^3 = (1 - \mathbf{M}_{bg})\mathbf{I}^1 + \mathbf{M}_{bg}\mathbf{I}_t^{1'}. \quad (4)$$

Fig. 2 illustrates an example of the third view synthesis. We can observe that using color transfer and context-aware blending could give a more realistic image composite.

C. Masked Sampling

Obtaining dense representations. The generated three views $\mathbf{I}^1, \mathbf{I}^2, \mathbf{I}^3$ are then encoded by a Siamese neural network f into dense representations $\mathbf{X}^i = f(\mathbf{I}^i), f(\mathbf{I}^i) \in \mathbb{R}^{H \times W \times C}, i \in \{1, 2, 3\}$. The resulting feature map has a size of $H \times W$ and a channel dimension C . Our encoder has a downsampling factor of 4. For more details see Sec. III-E.

Please note that we do not apply global average pooling to the dense representations. Instead of constraining the image-level consistency between different views, we perform pixel-level consistency via sampling multiple corresponding points in the overlapped area across views. Our intuition is that the learned spatially-sensitive features may better reduce the gap between the pre-training and downstream dense prediction CD task that requires spatially-variant representations. Moreover, we introduce the semantic mask to achieve class-balanced sampling, i.e., an equal number of points is randomly sampled for each semantic region in the overlapped area. The details of our dense representation learning based on masked sampling on the generated views for each sample are illustrated in Algorithm 2.

Algorithm 1: Views generation for a batch of samples

Input: $\hat{\mathbf{I}} \in \mathbb{R}^{B \times H_0 \times W_0 \times 3}$ (a batch of input images)
Input: $\hat{\mathbf{M}} \in \mathbb{R}^{B \times H_0 \times W_0}$ (a batch of corresponding semantic masks)
Output: $\hat{\mathbf{I}}^1, \hat{\mathbf{I}}^2, \hat{\mathbf{I}}^3 \in \mathbb{R}^{B \times H_0 \times W_0 \times 3}$ (a batch of image view 1/2/3)

```

1 // views generation for each sample in the batch
2 for b in 1 : B do
3   // generate view 1 and view 2 of the current image
4    $\hat{\mathbf{I}}^1[b], \hat{\mathbf{I}}^2[b] \leftarrow \mathcal{T}(\hat{\mathbf{I}}[b]), \mathcal{T}'(\hat{\mathbf{I}}[b])$ 
5    $\hat{\mathbf{M}}^1[b], \hat{\mathbf{M}}^2[b] \leftarrow \mathcal{T}_g(\hat{\mathbf{M}}[b]), \mathcal{T}'_g(\hat{\mathbf{M}}[b])$ 
6 end
7 for b in 1 : B do
8   // generate view 3 of the current image
9   // set the sample of an inverted index as the
    background image/mask
10   $\mathbf{I}^{1'} \leftarrow \hat{\mathbf{I}}^1[B - b]$ 
11   $\mathbf{M}^{1'} \leftarrow \hat{\mathbf{M}}^1[B - b]$ 
12   $\mathbf{I}_t^{1'} \leftarrow \text{ColorTransfer}(\mathbf{I}^{1'}, \hat{\mathbf{I}}^1[b])$ 
13  // obtain the common background mask
14   $\mathbf{M}_{bg} \leftarrow (\hat{\mathbf{M}}^1[b] == 0) \cdot (\mathbf{M}^{1'} == 0)$ 
15  // context-aware blending
16   $\mathbf{M}_{bg} \leftarrow \text{Erosion}(\mathbf{M}_{bg})$ 
17   $\hat{\mathbf{I}}^3[b] \leftarrow (1 - \mathbf{M}_{bg})\hat{\mathbf{I}}^1 + \mathbf{M}_{bg}\mathbf{I}_t^{1'}$ 
18 end

```

Overlapped region between views. Different views (view 1 and view 2) may correspond to different spatial areas in the original image due to applied geometry augmentations. In order to perform point consistency, we need first to obtain the overlapped region between \mathbf{I}^1 and \mathbf{I}^2 . Given the known geometry augmentations (\mathcal{T}_g and \mathcal{T}'_g), we could calculate the corresponding bounding box region ($BB^i = (u^i, v^i, w^i, h^i)$) of view $i, i \in \{1, 2\}$ in the original image \mathbf{I} by utilizing the parameters of each geometry augmentation (e.g., random cropping and random flipping) in the inverse order. For example, random cropping gives the upper-left coordinate (u, v) , the width w , and the height h of the cropped area in the input image. The overlapped region BB is the intersection of the two bounding box regions BB^1 and BB^2 . The region within BB defines the valid sampling region and other regions outside BB are invalid for the latter point sampling process.

Please note that we do not consider view 3 for calculating the overlapping region because we only take care of the foreground of view 3, which is shared with view 1.

Fig. 3 (a) gives an example of the visualization of the view correspondence. View 1 (\mathbf{I}^1) and view 2 (\mathbf{I}^2) respectively correspond to the region within the green/yellow bounding box in the original image \mathbf{I} . The overlapped area between views in form of bounding boxes (red) is shown in Fig. 3 (b).

Point sampling in the overlapped region. We sample N points $P_{kn} = (u_{kn}, v_{kn})$ with replacement for each semantic category k in the overlapping region, where (u_{kn}, v_{kn}) denotes the upper-left coordinate of the point P_{kn} in the original image/mask (\mathbf{I}/\mathbf{M}). N is the number of sampled points for each

Algorithm 2: Dense representation learning based on masked sampling for one sample

Input: $\mathbf{I}^1, \mathbf{I}^2, \mathbf{I}^3 \in \mathbb{R}^{B \times H_0 \times W_0 \times 3}$ (image view 1/2/3)
Input: $\mathbf{M} \in \mathbb{R}^{B \times H_0 \times W_0}$ (semantic mask of the image)
Input: $\mathcal{T}_g, \mathcal{T}'_g$ (applied geometry augmentations for the input)
Output: $\mathcal{L} \in \mathbb{R}$ (the loss on the input sample)

```

1 // reverse the area in input corresponding to view 1/2
2  $BB^1, BB^2 \leftarrow \text{Reverse}(\mathcal{T}_g), \text{Reverse}(\mathcal{T}'_g)$ 
3 // obtain overlapped region (BB) between views
4  $BB \leftarrow \text{Overlap}(BB^1, BB^2)$ 
5 // sampling N points in BB for each semantic category
6 for  $k$  in 1 : 2 do
7   for  $n$  in 1 : N do
8     sample  $P_{kn} \sim \text{Uniform}(\{p = (u, v) | p \text{ in } BB, \mathbf{M}[u][v] = k - 1\})$ 
9   end
10 end
11 // define the sampled point set
12  $P \triangleq \{P_{kn} | n \in \{1, 2, \dots, N\}, k \in \{1, 2\}\}$ 
13 // obtain cooresponding points in each view
14  $P^1, P^2 \leftarrow \mathcal{T}_g(P), \mathcal{T}'_g(P)$ 
15  $P^3 \leftarrow \{P^1_{kn} | n \in \{1, 2, \dots, N\}, k = 2\}$ 
16 // coordinates downscaling
17  $P^1, P^2, P^3 \leftarrow P^1 // ds, P^2 // ds, P^3 // ds$ 
18 // obtain point representations for each view
19 for  $i$  in 1 : 3 do
20    $\mathbf{X}^i \leftarrow f(\mathbf{I}^i)$ 
21    $\mathbf{x}^i \leftarrow \text{gather}(\mathbf{X}^i, P^i)$ 
22   // obtain projections/predictions
23    $\mathbf{z}^i \leftarrow g(\mathbf{x}^i)$ 
24    $\mathbf{p}^i \leftarrow h(\mathbf{z}^i)$ 
25 end
26 // compute losses
27 // loss1: distinguish foreground and background
28 for  $i$  in 1 : 2 do
29   for  $n$  in 1 : N do
30      $\mathcal{L}_{sd,n}^i \leftarrow \mathcal{D}(\mathbf{x}_{1n}^i, \mathbf{x}_{2n}^i) + 1$ 
31   end
32 end
33  $\mathcal{L}_{sd} \leftarrow \frac{1}{2N} \sum_{i=1}^2 \sum_{n=1}^N \mathcal{L}_{sd,n}^i$ 
34 // loss2: consistency between view 1/2
35 for  $k$  in 1 : 2 do
36   for  $n$  in 1 : N do
37      $\mathcal{L}_{s,kn}^{(1,2)} \leftarrow 1 - \frac{1}{2}(\mathcal{D}(\mathbf{p}_{kn}^1, \text{stopgrad}(\mathbf{z}_{kn}^2)) + \mathcal{D}(\mathbf{p}_{kn}^2, \text{stopgrad}(\mathbf{z}_{kn}^1)))$ 
38   end
39 end
40 end
41  $\mathcal{L}_{s1} \leftarrow \frac{1}{2N} \sum_{k=1}^2 \sum_{n=1}^N \mathcal{L}_{s,kn}^{(1,2)}$ 
42 // loss3: foreground consistency between view 1/3
43 for  $n$  in 1 : N do
44    $\mathcal{L}_{s,2n}^{(1,3)} \leftarrow 1 - \frac{1}{2}(\mathcal{D}(\mathbf{p}_{2n}^1, \text{stopgrad}(\mathbf{z}_{2n}^3)) + \mathcal{D}(\mathbf{p}_{2n}^3, \text{stopgrad}(\mathbf{z}_{2n}^1)))$ 
45 end
46 end
47  $\mathcal{L}_{s2} \leftarrow \frac{1}{N} \sum_{n=1}^N \mathcal{L}_{s,2n}^{(1,3)}$ 
48  $\mathcal{L} \leftarrow \mathcal{L}_{sd} + \mathcal{L}_{s1} + \mathcal{L}_{s2}$ 
  
```

class. Our default N is set to 16 (See Sec. III-E). $k=1$ denotes the background and $k=2$ denotes the foreground class. Let $P = \{P_{kn} = (u_{kn}, v_{kn}) | n \in \{1, 2, \dots, N\}, k \in \{1, 2\}\}$ denote the sampled point set. The corresponding points in view 1 and view 2 can be obtained by coordinate transformation under the given geometry augmentations:

$$\begin{aligned} P^1 &= \mathcal{T}_g(P) \\ P^2 &= \mathcal{T}'_g(P) \end{aligned} \quad (5)$$

where $P^i = \{P^i_{kn} = (u^i_{kn}, v^i_{kn}) | n \in \{1, 2, \dots, N\}, k \in \{1, 2\}\}$ denotes the set of coordinates of the sampled point in view $i, i \in \{1, 2\}$. Note that we divide P^i by ds (i.e., the down-sampling factor of the encoder, defaults to 4) to match the coordinates of the per-pixel representations \mathbf{X}^i . The sampled points set for view 3 is given by $P^3 = \{P^3_{kn} = P^1_{kn} | n \in \{1, 2, \dots, N\}, k = 2\}$.

Then for each view $i, i \in \{1, 2\}$, we gather N representations \mathbf{x}^i_{kn} in the embedding space $\mathcal{V} \in \mathbb{R}^C$ for each semantic category k by indexing points on the feature map \mathbf{x}^i using coordinates P^i :

$$\mathbf{x}^i = \text{gather}(\mathbf{X}^i, P^i) \quad (6)$$

where $\mathbf{x}^i = \{\mathbf{x}^i_{kn} | n \in \{1, 2, \dots, N\}, k \in \{1, 2\}\}$ represents the set of representations of sampled points for view i .

Similarly, we gather N representations \mathbf{x}^3_{kn} for view 3 using sampled points P^3 that belong to the region of the foreground class ($k=2$). Formally, $\mathbf{x}^3 = \{\mathbf{x}^3_{kn} | n \in \{1, 2, \dots, N\}, k = 2\}$.

D. Representation Learning

Towards discriminative features. Although representations of different semantic regions are decoupled from the dense feature map, the relationship between them is not fully utilized. To fully exploit the supervision of semantic relations, we employ a simple cosine-similarity-based loss to push away representations of points that belong to different semantic regions in the same image. Our motivation is the learned discriminative dense features could distinguish the objects of interest and other unconcerned backgrounds, which may facilitate the downstream change recognition of the interest land covers.

To achieve this, we enlarge the angle between the two selected vectors (i.e., point representations from the foreground and the background, respectively) in the embedding space \mathcal{V} by minimizing their cosine similarity. For simplicity, we construct N pairs of points by one-to-one correspondence between N foreground points \mathbf{x}^i_{2n} and N background points $\mathbf{x}^i_{1n}, n \in \{1, \dots, N\}$ for each view $i \in \{1, 2\}$. Note that we supplement 1 to cosine similarity to ensure a non-negative loss value. Our semantic dissimilar loss $\mathcal{L}_{sd,n}^i$ on one constructed point pair indexed n for view i is defined as follows:

$$\mathcal{L}_{sd,n}^i = \mathcal{D}(\mathbf{x}_{1n}^i, \mathbf{x}_{2n}^i) + 1 \quad (7)$$

where $\mathcal{D}(\cdot, \cdot)$ denotes the cosine similarity, given by:

$$\mathcal{D}(a, b) = \frac{a}{\|a\|_2} \cdot \frac{b}{\|b\|_2} \quad (8)$$

where $\|\cdot\|_2$ denotes ℓ_2 -norm, a, b are two vectors of the same dimension.

The semantic dissimilar loss for one sample is the average of $\mathcal{L}_{sd,n}^i$ on all the constructed point pairs in each view:

$$\mathcal{L}_{sd} = \frac{1}{2N} \sum_{i=1}^2 \sum_{n=1}^N \mathcal{L}_{sd,n}^i. \quad (9)$$

Cross-view similarity. Given the sampled points from different views, we constrain the similarity between their representations across different views by utilizing the cross-view spatial correspondence of the points. We aim to learn two kinds of point consistency: 1) consistency representations invariant to illumination changes, and 2) consistency foreground representations regardless of background changes. We employ view 1/2 to achieve the first kind consistency and view 1/3 for the second kind.

MLP-based projection/prediction networks are applied to representations to achieve consistency between the cross-view representations. For each view $i \in \{1, 2, 3\}$, the sampled point representations \mathbf{x}_{kn}^i from the encoder are projected into a subspace $\mathcal{Z} \in \mathbb{R}^{C'}$ by a projection MLP head (projector) $g: \mathcal{V} \mapsto \mathcal{Z}$ to obtain projection vectors $\mathbf{z}_{kn}^i = g(\mathbf{x}_{kn}^i)$. A prediction MLP head (predictor) $h: \mathcal{Z} \mapsto \mathcal{Z}$ transforms the output of one view (e.g., \mathbf{z}_{kn}^1) to obtain a prediction vector (e.g., $\mathbf{p}_{kn}^1 = h(\mathbf{z}_{kn}^1) \in \mathbb{R}^{C'}$) in the same space and matches it to the other view (e.g., \mathbf{z}_{kn}^2). We minimize the negative cosine similarity of representations of corresponding points between the two views i/i' . We define a symmetrized similarity loss for n th point of semantic category k between view i and view i' as follows:

$$\mathcal{L}_{s,kn}^{(i,i')} = 1 - \frac{1}{2} (\mathcal{D}(\mathbf{p}_{kn}^i, \text{stopgrad}(\mathbf{z}_{kn}^{i'})) + \mathcal{D}(\mathbf{p}_{kn}^{i'}, \text{stopgrad}(\mathbf{z}_{kn}^i))) \quad (10)$$

where $\text{stopgrad}(\cdot)$ means a stop-gradient operation. The encoder and projector can not receive gradient from projection vectors. Previous work [21] shows such operation is vital to prevent model collapse.

The first consistency loss is the average similarity loss between view 1 and view 2 on all the sampled points $n \in \{1, \dots, N\}$ for each semantic category $k \in \{1, 2\}$:

$$\mathcal{L}_{s1} = \frac{1}{2N} \sum_{k=1}^2 \sum_{n=1}^N \mathcal{L}_{s,kn}^{(1,2)}. \quad (11)$$

Similarly, the second consistency loss is the average similarity loss between view 1 and view 3 on all the sampled points $n \in \{1, \dots, N\}$ that belong to the foreground ($k=2$):

$$\mathcal{L}_{s2} = \frac{1}{N} \sum_{n=1}^N \mathcal{L}_{s,2n}^{(1,3)}. \quad (12)$$

Overall loss function. We calculate the summation of the semantic dissimilar loss and the two kinds of similarity losses to obtain our overall loss:

$$\mathcal{L} = \mathcal{L}_{sd} + \mathcal{L}_{s1} + \mathcal{L}_{s2}. \quad (13)$$

This is defined for each sample, and the total loss is averaged over all samples in a mini-batch.

E. Implementation Details

Encoder. We use the ResNet-18 [68] backbone (without fully connected layers and global pooling) equipped with Feature Pyramid Networks (FPN) [69] as our default encoder f to generate high-resolution and high-level per-pixel features for each image view. The ResNet-18 has 5 stages, each with downsampling by 2. Through the feedforward computation of the backbone, we obtain a feature hierarchy consisting of feature maps at different scales from the activation outputs of the last four stages. The FPN takes as input the feature hierarchy and progressively upsamples the coarse-resolution feature maps while merging them with the corresponding intermediate feature maps by element-wise addition. Each intermediate feature map undergoes a 1×1 convolutional layer to transform to the same channel dimension C before addition. The resulting feature map has a downsampling factor of 4 of the input image. The channel dimension C of output features is set to 256.

Projector. The projector g is 2-layer MLPs with a hidden dimension of 2048 and an output dimension of 1024. BN and ReLU are added between fully connected (fc) layers.

Predictor. The predictor h is 2-layer MLPs with a hidden dimension of 256 and an output dimension of 1024. BN and ReLU are also added between the two fc layers.

Data augmentation. We set probability of color jittering to 0.8, with {brightness, contrast, saturation, hue} strength of {0.4, 0.4, 0.4, 0.1}, and the probability of Gaussian blurring to 0.5 with a kernel std in [0.1, 2.0]. Geometric augmentation includes random vertical flip, random horizontal flip, and random resized crop with scale in [0.8, 1.0]. Note that we do not follow the common scale [21] for the random crop (i.e., [0.2, 1.0]) because the cropped two regions with a small scale may not contain an overlapped area, which may be detrimental to the effective sampling of spatially-aligned points across views.

Optimizer. We use Stochastic Gradient Descent (SGD) with a base learning rate of 0.01 for pre-training. The learning rate has a poly decay schedule [70]. The default number of pre-training epochs N_e is 200 (see Sec. IV-E). We set the weight decay to 0.0005 and the SGD momentum to 0.9. Due to capacity limitations of memory, the default batch size is set to 64. Our models are implemented on PyTorch and trained using a single NVIDIA RTX 3090 GPU.

IV. EXPERIMENTAL RESULTS

A. Pre-training Setup

Pre-training Dataset. We leverage image-label pairs from the existing Inria building labeling dataset [34], which provides 180 labeled RS images, each size of 5000×5000 and spatial resolution of 0.3 m. The data is labeled into the building and non-building classes. We cut the original samples into small patches of size 256×256 with no overlap and remove patches not containing building regions. The resulting dataset contains more than 45k patch samples. We randomly split it into training (80%) and validation sets (20%). We additionally obtain the co-registered image patch of the corresponding

geospatial region via Google Earth as the temporal augmentation (t_2) for each image patch (t_1) in the dataset. For a fair comparison, the natural augmentations (bitemporal images) are used to train some other related pre-training methods that learn season invariant features. Please note that the semantic mask may not perfectly match the image of t_2 due to land-cover changes (e.g., building construction and demolition) over time, we do not include the augmented temporal image in our pre-training framework.

B. Downstream Change Detection Setup

1) *Change detection datasets*: To evaluate the pre-trained model, we conduct experiments on the following three change detection datasets:

LEVIR-CD [2]: a widely-used building change detection dataset. LEVIR-CD contains 637 pairs of bitemporal VHR RS images, each with a size of 1024×1024 and a spatial resolution of 0.5m. We follow the default train-valid-test split [2]. Each image is cut into small patches of size 256×256 with no overlap. Finally, we obtain 7120/1024/2048 samples for training/validation/testing, respectively.

WHU-CD [35]: a public building change detection dataset that includes one pair of optical VHR RS aerial images with a size of 32507×15354 and 0.075m spatial resolution. Similarly, we crop the original sample into small patches of size 256×256 with no overlap. We randomly split the dataset into training, validation, and testing sets, with 6096/762/762 samples, respectively.

Guangzhou-CD [36]: a building change detection dataset that covers several suburb areas of Guangzhou City, China. It contains 19 VHR RGB image pairs (0.55m) with sizes ranging from 1006×1168 to 4936×5224 pixels. Similarly, the image pairs are cropped into 256×256 non-overlapping patches. As the dataset provider does not give a default dataset split, we randomly split the dataset into three parts, with 2882/361/360 samples for training, validation, and testing, respectively.

2) *Change detection networks*: We employ a simple yet effective change detection model [38] which consists of a Siamese feature extractor (deep FCN) to extract high-resolution semantic feature maps for bitemporal patches, a distance metric to calculate the Feature Difference Images (FDI) between the two patches, and a relatively shadow FCN to give the change probability maps. Differently, we use a more light FPN-based decoder head [69] for the feature extractor with an encoder-decoder structure. Our change detection networks employ a ResNet-18 backbone. We use the cross-entropy loss to optimize our CD model. Please refer to [38] for more details.

Fine-tuning details. We fine-tune the downstream CD networks using the pre-trained models. For a fair comparison, we only initialize the backbone (i.e., Resnet-18) of the CD networks by that from the pre-trained model. Note that the parameters of other components of the CD networks are initialized with zero-mean normal distribution with a standard deviation of 0.02.

Training details. We apply data augmentation, including random flip, and Gaussian blur. Batch size is set to 8. SGD is

used for model optimization. We set the momentum to 0.9 and the weight decay to 0.0005. The learning rate starts at 0.01 and linearly decays to 0 in 200 epochs. We perform validation after each training epoch, and use the best model on the validation set for evaluation on the test set.

Evaluation Metrics. We use the F1-score with regard to the change category as the evaluation indices. Additionally, precision, recall, Intersection over Union (IoU) of the change category are also reported. The above metrics are defined as follows:

$$\begin{aligned} \text{F1} &= \frac{2}{\text{recall}^{-1} + \text{precision}^{-1}} \\ \text{precision} &= \frac{\text{TP}}{\text{TP} + \text{FP}} \\ \text{recall} &= \frac{\text{TP}}{\text{TP} + \text{FN}} \\ \text{IoU} &= \frac{\text{TP}}{\text{TP} + \text{FN} + \text{FP}} \end{aligned} \quad (14)$$

where TP, FP, FN denote the number of true positive, false positive, and false negative respectively.

C. Overall Comparison

To evaluate the effectiveness of our proposed pre-trained model, we make a comparison with several baselines, including random initialization, ImageNet pre-training, in-domain supervised pre-training, and several self-supervised pre-training methods:

- *Random initialization*. All the parameters of the CD networks are initialized by the zero-mean normal distribution with a deviation of 0.02.
- *ImageNet pre-training*. The backbone (ResNet-18) of our CD model is initialized with the ImageNet pre-training.
- *In-domain supervised pre-training (In-domain Sup.)*: We employ an FCN-based semantic segmentation network with a ResNet-18 backbone and an FPN head [69], supervised by the image-mask pairs from our pre-training dataset. We follow the same optimization configuration as that for CD networks. We perform the model evaluation in the validation set after each training epoch and save the best model (backbone) for the downstream task.
- *SimSiam* [21]: A popular SSL method without using negative samples. SimSiam employs stop-gradient and predictor to prevent model collapse.
- *MoCo-v2* [56]: A competitive SSL model that learns meaningful representations by formulating contrastive learning as a dictionary look-up problem on a dynamic queue that covers a large set of negative samples.
- *DenseCL* [58]: A dense contrastive learning method that constrains the pixel-level cross-view consistency where the pixel correspondence is computed via traversing pairwise similarity between pixels from different views.
- *CMC* [29]: A recent SSL method in RS that takes the semantic mask as an additional view along with the ordinary image to learn consistent cross-modal representations under the framework of contrastive multiview coding [71].

- *SeCo* [16]: A very recent SSL method that is based on MoCo-v2 and exploits the use of multi-temporal RS images as natural augmentations to learn seasonal invariant representations.

For a fair comparison, we use our pre-training dataset for self-supervised pre-training for SimSiam, MoCo-v2, DenseCL, CMC, and SeCo. We implement these SSL methods using their public codes with default hyperparameters. Note that all the compared SSL models are initialized with ImageNet pre-trained weights as our SaDL does.

Each pre-trained model is evaluated by the performance of the CD model on the CD task. We use the same CD networks for each pre-trained model. We show their performance under different regimes of the labeled CD data. We set a variety of data conditions: 1%, 5%, 20%, and 100%, each of which represents a proportion of available labeled training data. Tab. I reports the overall comparisons of our proposed method and other pre-trained models on the LEVIR-CD, WHU-CD, and Guangzhou-CD datasets, respectively. Precision, recall, F1-score, and IoU of the CD networks on the three CD test sets are given. Visualization comparison of the prediction CD results on the three datasets for each pre-trained model is also given in Fig. 4.

From Tab. I, we can observe that the proposed method consistently outperforms the compared pre-trained models on the three datasets, especially in the small data regimes. Specifically, our SaDL pre-training is significantly superior to random initiation. It is notable that we can achieve comparable or even better results with only 20% training data than the random initiation baseline using 100% training data. It indicates that our pre-training can effectively alleviate the small labeled data problem.

ImageNet pre-training serves as a strong baseline and is widely used to see the gap between supervised and unsupervised pre-training. Our method induces further improvements against ImageNet pre-training. For instance, Tab. I (a) shows compared to ImageNet, we achieve an improvement of more than 100% on the F1-score in the LEVIR-CD test set under small data conditions (1% and 5%).

Comparison to in-domain supervision. In-domain supervised (sup.) pre-training aims to obtain in-domain discriminative representations by learning the mapping from RS images to labels. Tab. I shows the in-domain supervision is consistently inferior to our SaDL under each data configuration of the three datasets, even not comparable to ImageNet pretraining in some data regimes. Note that we use the same amount of pre-training data for SaDL and in-domain supervision. Our empirical results indicate that our SaDL can learn more transferable features than supervised pre-training. We can observe that in-domain supervision shows relatively poorer results on the WHU-CD/Guangzhou-CD datasets than on the LEVIR-CD dataset. It is because subdomain diversity may be present in different RS datasets. The traditional supervised pre-training may overfit patterns in a certain domain and lack transferability to another.

Comparison to other SSL pretraining. Tab. I also illustrates that our method consistently outperforms several SSL methods, including two popular image-level representation

learning methods, one dense contrastive learning method, and two recent SSL methods in the RS domain. We can observe that the normal dense contrastive learning (DenseCL) can even be inferior to the image-level counterpart (MoCo) in many data conditions. It may due to the discrepancy between the widely applied ImageNet image and the ordinary RS image. Different from the ImageNet data that mainly contains one object in the center of the image, there may exist multiple similar foreground objects at different spatial locations in an RS image. The intrinsic characteristic of RS data brings difficulty in computing pixel correspondence cross views by comparing dense feature similarities for DenseCL. The resulting incorrect correspondence may hinder learning meaningful representations. On the contrary, we utilize the correct pixel correspondence for representation learning where the corresponding pixels are obtained by leveraging geometry transformations on the pixels of the overlapped area between views.

The comparison results with CMC indicate that we exploit a better approach to using the semantic mask as additional information in a self-supervised learning framework to improve feature representations. We argue that directly using the mask as an augmented view along with the image views may not be an optimal solution. In [29], the mask is encoded into one pooled vector that losses spatial semantic details. The semantic relation has not been fully utilized in such a scenario. Instead, we leverage semantic masks to push away representations of pixels from different semantic regions to learn semantic-aware features that can distinguish the foreground or background pixels, thus benefiting the recognition of objects of interest in the downstream CD task.

Fast convergence To further show the transferability of pre-trained models, Fig. 5 illustrates the validation accuracy (mean F1-score) for each training epoch on the downstream CD task using 5% LEVIR-CD/WHU-CD/Guangzhou-CD training data. We can observe that our SaDL outperforms the baselines on validation accuracy in terms of stability and effectiveness. It indicates that our method provides better model initialization, which accelerates fine-tuning convergence and incurs better performance on the downstream CD task.

D. Ablation Studies

We conduct ablation studies on the three key components of our proposed SaDL: 1) dense representation learning via masked-based point sampling (MS), 2) learning discriminative features via semantic discrimination (SD), and 3) learning consistent foreground features via background swap (BS). We start from the SimSiam [21] with an FPN-based encoder, which learns consistent features between two artificially augmented views of the same image, as our baseline. We incrementally add the three key components to the baseline to evaluate their respective gains to the performance of the model. All the above models are trained on our pre-training dataset for 200 epochs and then transferred to the downstream CD task. Downstream experiments are performed under the 5% data regime of the LEVIR-CD/WHU-CD/Guangzhou-CD datasets.

Ablation on masked sampling. Quantitative results in Tab. II illustrates that our dense representation learning via

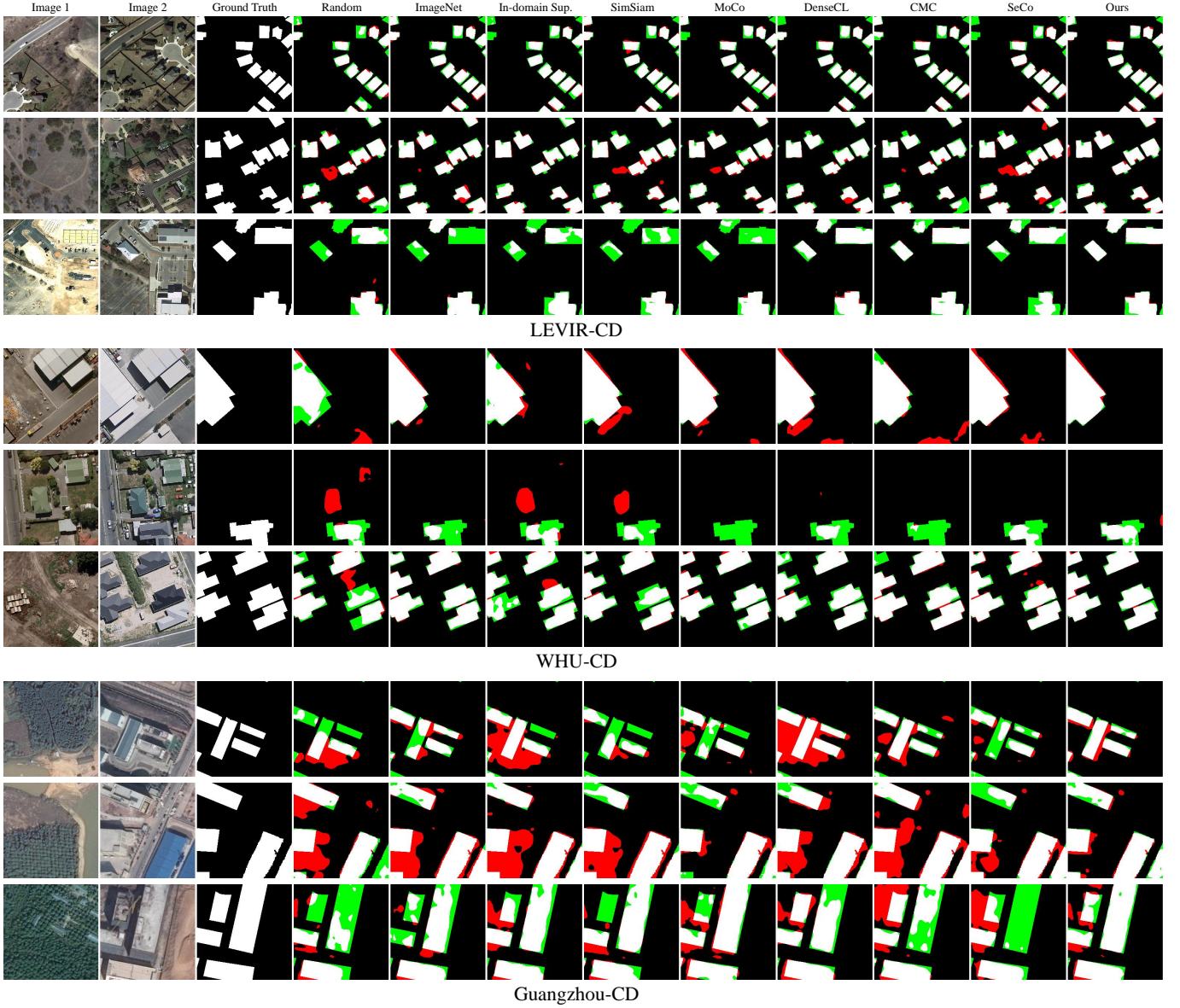


Fig. 4. Visualization comparison of the CD model fine-tuned from different pre-trained models on the LEVIR-CD/WHU-CD/Guangzhou-CD test sets. The CD model is trained under a 20% data regime.

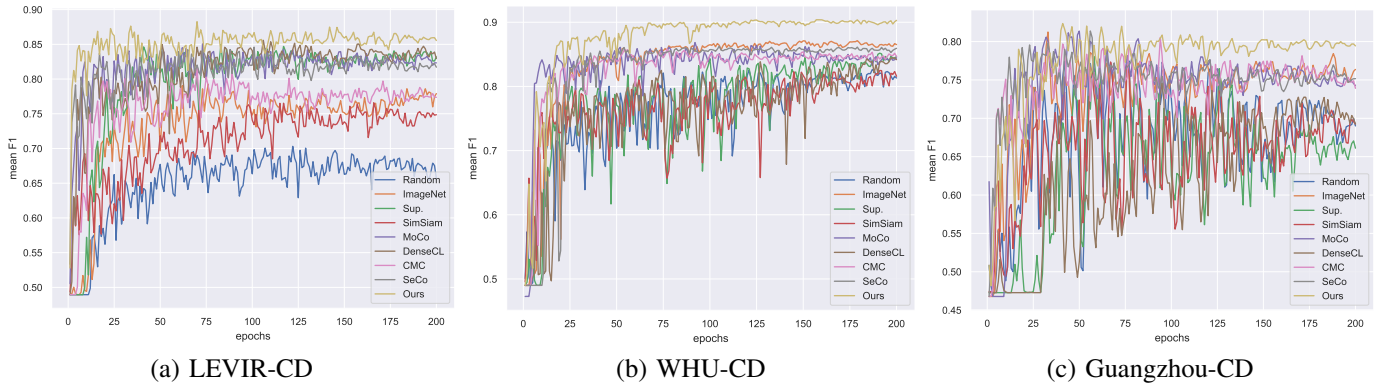


Fig. 5. Accuracy of CD models for each training epoch. The mean F1-score is reported.

TABLE I

OVERALL COMPARISONS OF DIFFERENT PRE-TRAINING METHODS ON THE THREE CD DATASET. PRECISION/RECALL/F1/IOU OF THE CD MODEL ON THE LEVIR-CD/WHU-CD/GUANGZHOU-CD TEST SET ARE REPORTED. THE HIGHEST CLASSIFICATION ACCURACY IN EACH DATA REGIME IS MARKED IN BOLD.

(a) LEVIR-CD				
	1%	5%	20%	100%
	Precision / Recall / F1 / IoU	Precision / Recall / F1 / IoU	Precision / Recall / F1 / IoU	Precision / Recall / F1 / IoU
Random ImageNet	49.83 / 13.56 / 21.32 / 11.93	73.54 / 34.58 / 47.05 / 30.76	83.00 / 77.76 / 80.30 / 67.08	90.50 / 84.94 / 87.63 / 77.98
In-domain Sup.	30.80 / 20.11 / 24.33 / 13.85	81.40 / 54.35 / 65.18 / 48.35	89.59 / 82.26 / 85.76 / 75.08	91.29 / 85.25 / 88.16 / 78.83
SimSiam [21]	79.43 / 17.96 / 29.29 / 17.16	86.25 / 61.73 / 71.96 / 56.20	90.91 / 81.02 / 85.68 / 74.95	91.22 / 85.11 / 88.06 / 78.67
MoCo-v2 [56]	71.90 / 13.29 / 22.44 / 12.64	82.46 / 44.41 / 57.73 / 40.58	88.97 / 76.46 / 82.24 / 69.84	91.47 / 84.78 / 88.00 / 78.57
DenseCL [58]	58.15 / 20.30 / 30.09 / 17.71	74.78 / 71.20 / 72.95 / 57.42	88.78 / 80.45 / 84.41 / 73.03	91.59 / 85.06 / 88.21 / 78.90
CMC [29]	72.45 / 28.76 / 41.17 / 25.92	91.51 / 58.62 / 71.46 / 55.60	89.33 / 82.09 / 85.56 / 74.76	94.63 / 79.98 / 86.69 / 76.51
SeCo [16]	79.43 / 10.42 / 18.42 / 10.15	84.45 / 56.40 / 67.63 / 51.09	90.30 / 77.94 / 83.67 / 71.92	90.73 / 86.59 / 88.61 / 79.55
	68.63 / 29.01 / 40.78 / 25.62	84.74 / 61.43 / 71.23 / 55.31	84.34 / 83.70 / 84.02 / 72.44	91.03 / 85.68 / 88.27 / 79.01
Ours	82.38 / 42.52 / 56.09 / 38.98	88.35 / 72.16 / 79.44 / 65.90	89.58 / 85.05 / 87.25 / 77.39	90.91 / 86.66 / 88.74 / 79.75
(b) WHU-CD				
	1%	5%	20%	100%
	Precision / Recall / F1 / IoU	Precision / Recall / F1 / IoU	Precision / Recall / F1 / IoU	Precision / Recall / F1 / IoU
Random ImageNet	37.03 / 41.76 / 39.25 / 24.42	67.99 / 64.40 / 66.14 / 49.41	70.07 / 72.68 / 71.35 / 55.46	85.82 / 83.20 / 84.49 / 73.15
In-domain Sup.	31.37 / 33.55 / 32.42 / 19.35	80.12 / 67.92 / 73.52 / 58.12	87.82 / 76.87 / 81.98 / 69.46	91.11 / 86.14 / 88.55 / 79.46
SimSiam [21]	43.41 / 60.49 / 50.55 / 33.82	74.50 / 66.06 / 70.03 / 53.88	70.79 / 72.34 / 71.56 / 55.71	84.10 / 82.42 / 83.25 / 71.31
MoCo-v2 [56]	37.86 / 47.38 / 42.09 / 26.65	60.37 / 73.03 / 66.10 / 49.36	70.89 / 76.11 / 73.41 / 57.99	86.30 / 83.14 / 84.69 / 73.45
DenseCL [58]	71.36 / 57.44 / 63.65 / 46.68	76.45 / 67.21 / 71.53 / 55.68	85.30 / 76.36 / 80.58 / 67.48	91.36 / 84.69 / 87.90 / 78.41
CMC [29]	41.02 / 46.45 / 43.56 / 27.85	68.78 / 69.05 / 68.92 / 52.58	84.14 / 74.37 / 78.95 / 65.22	89.38 / 84.64 / 86.94 / 76.90
SeCo [16]	50.89 / 45.32 / 47.94 / 31.53	73.69 / 67.54 / 70.49 / 54.42	86.28 / 74.54 / 79.98 / 66.64	89.96 / 85.47 / 87.66 / 78.03
	67.39 / 41.92 / 51.68 / 34.85	78.81 / 66.52 / 72.15 / 56.43	83.93 / 76.43 / 80.00 / 66.67	89.29 / 86.93 / 88.09 / 78.72
Ours	78.50 / 66.29 / 71.88 / 56.10	86.45 / 75.04 / 80.34 / 67.15	90.15 / 81.37 / 85.53 / 74.73	93.10 / 87.05 / 89.98 / 81.78
(c) Guangzhou-CD				
	1%	5%	20%	100%
	Precision / Recall / F1 / IoU	Precision / Recall / F1 / IoU	Precision / Recall / F1 / IoU	Precision / Recall / F1 / IoU
Random ImageNet	40.42 / 51.63 / 45.34 / 29.32	62.33 / 50.03 / 55.51 / 38.42	72.89 / 54.51 / 62.37 / 45.32	91.80 / 65.02 / 76.12 / 61.45
In-domain Sup.	52.68 / 38.36 / 44.39 / 28.53	62.54 / 57.82 / 60.09 / 42.94	88.93 / 59.59 / 71.36 / 55.48	94.99 / 76.81 / 84.94 / 73.82
SimSiam [21]	36.54 / 51.99 / 42.92 / 27.32	66.53 / 42.04 / 51.52 / 34.70	69.82 / 60.43 / 64.79 / 47.91	88.96 / 73.11 / 80.26 / 67.03
MoCo-v2 [56]	42.40 / 51.09 / 46.34 / 30.16	73.02 / 43.49 / 54.51 / 37.47	67.29 / 61.14 / 64.07 / 47.13	91.80 / 72.60 / 81.08 / 68.18
DenseCL [58]	50.73 / 48.56 / 49.62 / 33.00	67.33 / 56.56 / 61.48 / 44.38	81.24 / 61.80 / 70.20 / 54.08	90.23 / 76.69 / 82.91 / 70.81
CMC [29]	37.06 / 51.16 / 42.98 / 27.37	58.69 / 40.78 / 48.12 / 31.69	77.36 / 57.88 / 66.21 / 49.49	93.19 / 71.36 / 80.83 / 67.82
SeCo [16]	46.77 / 38.94 / 42.50 / 26.98	75.17 / 53.37 / 62.42 / 45.37	73.97 / 66.46 / 70.01 / 53.86	92.20 / 76.72 / 83.75 / 72.04
	46.75 / 50.62 / 48.61 / 32.11	63.50 / 56.70 / 59.91 / 42.76	80.08 / 60.62 / 69.00 / 52.68	92.51 / 76.98 / 84.03 / 72.46
Ours	57.96 / 47.79 / 52.39 / 35.49	80.04 / 56.00 / 65.89 / 49.13	85.32 / 67.06 / 75.09 / 60.12	92.13 / 81.06 / 86.24 / 75.81

sampling multiple points for each semantic category brings consistent and significant performance improvements across the three datasets, compared to the baseline. It indicates that our masked sampled point-based solution introduces much more valuable information to representation learning than the traditional global average pooling-based counterpart that loses spatial details. Moreover, we also make a comparison to the masked pooling-based approach [53], which pools features belonging to each semantic region into one semantic vector by leveraging the semantic mask. Simply constraining each semantic vector invariant across views brings small improvement, compared to the global pooling approach (baseline). We can observe that our sampling-based method is far superior to the masked pool one. The multiple pixel correspondences across views through masked sampling provide more diverse supervision of spatial accordance, thus benefiting representation learning.

Ablation on semantic discrimination. To make full use

of the semantic mask, we employ the additional loss term, namely semantic dissimilarity loss, to learn discriminative features that can distinguish pixels from different semantic categories. Tab. II shows that our SD induces considerable improvements in the F1-score of the pre-trained CD model across the three datasets. The empirical results indicate that our semantic discrimination can significantly improve the model transferability. It may attribute to the role of the semantic mask in our SSL framework. We include the supervision of the semantic mask into our pre-training in a contrastive manner. Different from directly learning the mapping from the image to the label, we enforce the model to learn discriminative features via pushing away representations between pixels from the foreground (i.e., buildings) and the background in an image by leveraging the semantic relations. The resulting model obtains discriminative features that could distinguish interest land covers from backgrounds, thus benefiting the recognition of change of interest in the downstream CD task.

TABLE II

ABLATION STUDIES OF OUR SaDL, INCLUDING 1) DENSE REPRESENTATION LEARNING VIA MASKED POINT SAMPLING (MS), 2) LEARNING DISCRIMINATIVE FEATURES VIA SEMANTIC DISCRIMINATION (SD), AND 3) LEARNING CONSISTENT FOREGROUND FEATURES VIA BACKGROUND SWAP (BS). THE F1-SCORE ON THE LEVIR-CD/WHU-CD/GZ-CD TEST SET IS REPORTED. THE CD MODEL IS TRAINED UNDER THE DATA REGIME OF 5%.

	MS	SD	BS	LEVIR	WHU	GZ
Baseline	×	×	×	60.69	64.53	48.24
+masked pool	×	×	×	63.09	66.03	48.64
Ours	✓	×	×	70.21	71.90	54.15
Ours	✓	✓	×	77.74	77.43	64.21
Ours	✓	✓	✓	79.44	80.34	65.89

TABLE III

EFFECT OF THE THIRD VIEW. THE F1-SCORE AND IOU ON THE LEVIR-CD/WHU-CD/GUANGZHOU-CD TEST SET ARE REPORTED. THE CD MODEL IS TRAINED UNDER THE DATA REGIME OF 5%.

	LEVIR-CD		WHU-CD		Guangzhou-CD	
	F1	IoU	F1	IoU	F1	IoU
base	77.74	63.58	77.43	63.17	64.21	47.29
+ natural	78.32	64.37	78.86	65.10	62.99	45.98
ours	79.44	65.90	80.34	67.15	65.89	49.13

Ablation on background swap. Apart from the traditional two artificial augmented views, we propose a third view via swapping the background of the current image from that of another one. This incurs an additional cross-view similarity loss, i.e., learning invariant foreground features between view 1 and view 3. Quantitative results in Tab. II demonstrate that our DS further brings consistent improvements in the performance of the pre-trained CD model on the three CD datasets. It indicates that the learned foreground representations invariant to background changes benefit the downstream change detection for the interest foreground land covers. Our background swap can be viewed as an approach to synthesizing unconcerned changes in a scene. Such design may enforce the model to focus more on the change of interest related to the foreground, but not irrelevant changes within the background. To further verify the effectiveness of introduced third view, we also compare the natural augmentation, i.e., augmenting the current view with a registered image from another temporal. For a fair comparison, we apply the same loss for constraining consistent foreground representations between view 1 and view 3. Tab. III demonstrates our synthetic view consistently outperforms the natural counterpart. While natural augmentation provides rich illumination changes, undesired real foreground changes could also occur, which may hinder representation learning.

E. Parameter Analysis

Sampled point number. The sampled number of points N for each semantic category is an important hyperparameter. We test different configurations of our SaDL containing varying sampled point numbers $N = \{1, 4, 16, 64\}$. We train each model 200 epochs on the same pre-training dataset. Tab. IV

TABLE IV

EFFECT OF SAMPLED POINT NUMBER N . THE F1-SCORE AND IOU ON THE LEVIR-CD/WHU-CD/GUANGZHOU-CD TEST SET ARE REPORTED. THE CD MODEL IS TRAINED UNDER THE DATA REGIME OF 5%.

	LEVIR-CD		WHU-CD		Guangzhou-CD	
N	F1	IoU	F1	IoU	F1	IoU
1	74.00	58.73	78.49	64.59	63.51	46.53
4	75.98	61.26	80.23	66.98	66.07	49.33
16	79.44	65.90	80.34	67.15	65.89	49.13
64	76.12	61.45	76.34	61.73	64.84	47.97

TABLE V

EFFECT OF THE NUMBER OF PRE-TRAINING EPOCHS. THE F1-SCORE AND IOU ON THE LEVIR-CD/WHU-CD/GUANGZHOU-CD TEST SETS ARE REPORTED. THE CD MODEL IS TRAINED UNDER THE DATA REGIME OF 5%.

	LEVIR-CD		WHU-CD		Guangzhou-CD	
epochs	F1	IoU	F1	IoU	F1	IoU
0	65.18	48.35	73.52	58.12	57.86	40.71
5	73.68	58.33	75.39	60.51	60.54	43.41
20	76.48	61.92	79.17	65.52	65.61	48.82
100	77.14	62.79	79.76	66.34	64.57	47.68
200	79.44	65.90	80.34	67.15	65.89	49.13
400	79.59	66.10	80.06	66.75	64.37	47.47

illustrates the effect of the sampled point number of the pre-trained model on the downstream transferring performance. We report the F1-score/IoU of the CD model trained on a 5% data regime of the LEVIR-CD/WHU-CD/Guangzhou-CD datasets. We can observe a significant improvement in the F1-score of the model when increasing the point number from 1 to 16. It is because that multiple sampled points from different spatial locations introduce more spatial-diverse information for both learning view-invariant and semantically-discriminative features. The learned illumination-invariant and semantic-aware representations could facilitate the change recognition in the downstream CD task. We can also observe a drop in F1-score when further increasing N from 16 to 64. It may be because the over-sampled points nearby the edge of the semantic regions could bring difficulty in training semantically-discriminative features. Therefore, we set N to 16.

Pre-training epochs number. The number of pre-training epochs N_e affects the quality of the pre-trained model. We train our SaDL using varying pre-training epochs numbers $N_e \in \{5, 20, 100, 200, 400\}$ and compare their performance on the downstream CD task. Tab. V reports the F1-score/IoU of each pre-trained CD model on the LEVIR-CD/WHU-CD/Guangzhou-CD datasets under a 5% data regime. Note that $N_e = 0$ denotes the ImageNet pre-training. We can observe a significant improvement in the F1-score even with a very small number of pre-training epochs (e.g., 5), compared to the baseline ($N_e = 0$). The performance of the CD model further increases with longer pre-training (e.g., from 5 to 200 epochs). We can also observe a negligible improvement or even some drops in the F1-score of the CD model on the

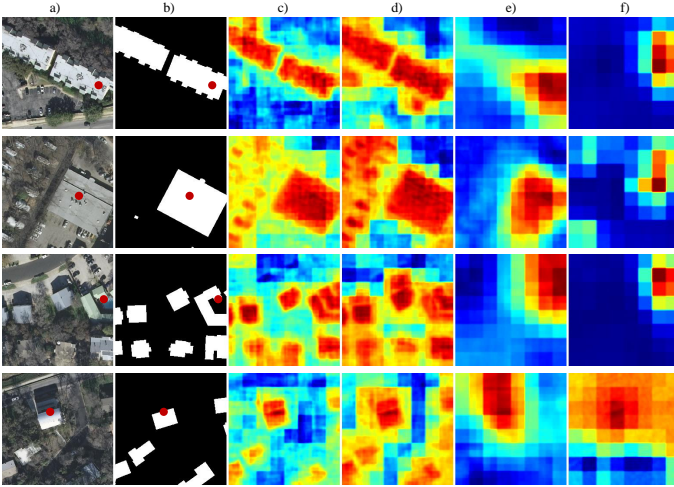


Fig. 6. Visualization of self-similarity map of our SaDL on the pre-training dataset. Given one selected point (viewed in red) in the a) image, we give visualization results of the ablation versions of our model, including f) baseline, e) ours with masked sampling (MS), d) ours with MS and semantic discrimination (SD), c) ours with MS, SD, and background swap (BS). The semantic mask b) is shown for a better view.

downstream tasks when further increasing the N_e from 200 to 400. A pre-training with too long training epochs may overfit the pre-training data and incur poorer model transferability. Therefore, we set N_e to 200.

F. Feature Visualization

1) *Encoder visualization*: We incorporate the semantic supervision of the mask into a self-supervised framework via masked sampling of semantically-meaningful pixel-wise features to learn semantic-aware dense representations. To better inspect the semantic information of the learned dense representations, we visualize the feature self-similarity map of the output dense per-pixel features from our encoder.

Feature self-similarity map. For one selected point on an image, we can obtain one self-similarity map by calculating the correlations between features of the selected point and all the other pixels in the image. Formally, given the per-pixel features $\mathbf{X} \in \mathbb{R}^{HW \times C}$ and one selected point feature $\mathbf{x} = \mathbf{X}[p] \in \mathbb{R}^C, p = (u, v)$, the self-similarity map $SM \in \mathbb{R}^{HW}$ of the point p is given by their dot product followed by softmax on the channel of HW , i.e., $SM = \text{softmax}(\mathbf{X} \cdot \mathbf{x})$.

Fig 6 shows some examples of self-similarity maps of the selected foreground points (viewed in red) on images in our pre-training dataset. Red denotes higher similarity values and blue denotes lower values. From Fig. 6 c), we can observe that the selected foreground point shows strong correlations with pixels of the same semantic category (building). It indicates that our SaDL can obtain high-resolution high-level features that can reveal semantic relations between pixels.

Fig. 6 also gives visualization results for other ablation versions of the proposed model, including our baseline [f)], baseline + MS [e)], and baseline + MS + SD [d)]. We can observe that ours with MS can highlight pixels nearby the selected point and shows a relatively more accurate location response than the baseline. It implies the effectiveness of

the proposed dense representation learning based on masked sampling over the traditional average pooling approach. Ours with MS can learn spatially sensitive features via leveraging valuable spatial information in location correspondences manner, instead of pooling the spatial features. We can also observe our ablation [d)] highlights more accurate foreground regions than that of e). It indicates our introduced SD incurs discriminative representations that well distinguish the foreground and the background. Moreover, our full SaDL model [c)] obtain more refined visualization results by further adding BS to learn consistent foreground features invariant to background changes.

2) *Backbone visualization*: For a fair comparison, we only transfer parameters of the backbone (i.e., ResNet-18) in our SaDL on the downstream CD model as in other pre-trained models. To interpret what concepts are learned by the networks, we compare the backbone visualization of each pre-trained model by utilizing network visualization techniques - Class Activation Maps (CAM) [72]. Basically, a CAM is the weighted sum of each channel activation map from a certain layer in the network. Here, we visualize the last convolution layer of the backbone.

Fig. 7 shows the comparison of CAM for different pre-trained models. Red denotes higher attention values and blue denotes lower values. We test images from both our pre-training dataset as well as the three downstream CD datasets. We can observe that the CAM of our model shows high concentrations at the foreground objects in the image with a satisfactory localization accuracy. It is notable that our model can not only attend to interest land covers on the pre-training images but also perform well on the downstream CD images that show significant domain gaps (e.g., differences in spatial resolution and style of the objects) from the pre-training data. For instance, the high-density buildings (see the last row in Fig. 7) in the Guangzhou-CD dataset are hardly present in the pre-training dataset. It indicates that our proposed pre-training could extract transferable semantically-meaningful representations with well generalization ability.

V. CONCLUSION

In this paper, we proposed a semantic-aware pre-training method for remote sensing image change detection. We incorporate the semantic information into a self-supervised learning framework to enhance the feature discrimination ability. Instead of manipulating the image-level features, we constrain pixel-level representation consistency based on sampling multiple points across views by introducing spatial-aligned location correspondences, thus obtaining spatially sensitive features benefiting the downstream dense prediction CD task. Apart from learning illumination invariant representations, we employ an additional loss term to learn discriminative features that can distinguish foreground land covers and other backgrounds. Moreover, we augment the third view via background swap to learn consistent foreground presentations regardless of irrelevant background changes. Extensive experiments on three downstream CD datasets verify the effectiveness of the proposed method. Our SaDL significantly outperforms

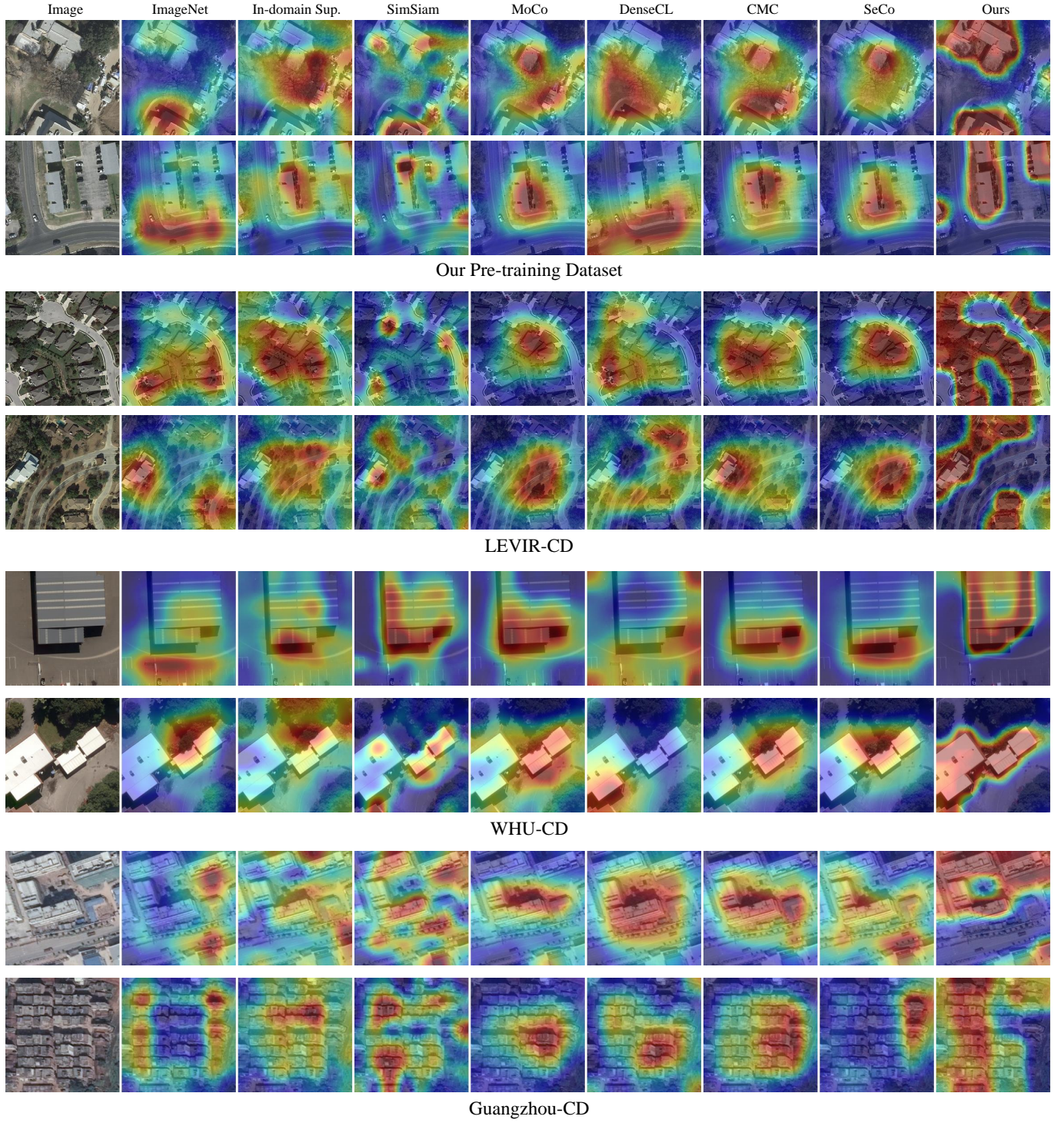


Fig. 7. Class activation maps of different pre-trained models. We test images from our pre-training dataset and the downstream LEVIR-CD/WHU-CD/Guangzhou-CD datasets.

ImageNet pre-training, in-domain supervised pre-training, and several SSL pre-training methods, especially in small data regimes. For example, ours surpasses the compared pre-training methods by a large margin (6% ~ 200%) in terms of F1-score under a 1% data regime. The empirical experiments indicate SaDL can well alleviate the data insufficiency in the CD task. Notably, we can achieve comparable or even better results using only 20% training data than the random initiation baseline using 100% data. The feature visualization results also demonstrate that our method can extract semantically-meaningful representations with well generalization ability on different downstream images that show domain discrepancies with the pre-training data.

REFERENCES

- [1] A. SINGH, "Review article digital change detection techniques using remotely-sensed data," *International Journal of Remote Sensing*, vol. 10, no. 6, pp. 989–1003, 1989. [Online]. Available: <https://doi.org/10.1080/01431168908903939>
- [2] H. Chen and Z. Shi, "A spatial-temporal attention-based method and a new dataset for remote sensing image change detection," *Remote. Sens.*, vol. 12, no. 10, p. 1662, 2020.
- [3] L. Bruzzone and D. Prieto, "Automatic analysis of the difference image for unsupervised change detection," *IEEE Transactions on Geoscience and Remote Sensing*, vol. 38, no. 3, pp. 1171–1182, 2000.
- [4] P. P. de Bem, O. A. de Carvalho Junior, R. F. Guimarães, and R. A. T. Gomes, "Change detection of deforestation in the brazilian amazon using landsat data and convolutional neural networks," *Remote Sensing*, vol. 12, no. 6, p. 901, 2020.
- [5] J. Z. Xu, W. Lu, Z. Li, P. Khaitan, and V. Zaytseva, "Building damage detection in satellite imagery using convolutional neural networks," 2019.
- [6] L. Bruzzone and F. Bovolo, "A novel framework for the design of change-detection systems for very-high-resolution remote sensing images," *Proceedings of the IEEE*, vol. 101, no. 3, pp. 609–630, 2013.
- [7] W. Shi, M. Zhang, R. Zhang, S. Chen, and Z. Zhan, "Change detection based on artificial intelligence: State-of-the-art and challenges," *Remote Sensing*, vol. 12, p. 1688, 5 2020.
- [8] M. Zhang, G. Xu, K. Chen, M. Yan, and X. Sun, "Triplet-based semantic relation learning for aerial remote sensing image change detection," *IEEE Geosci. Remote. Sens. Lett.*, vol. 16, no. 2, pp. 266–270, 2019.
- [9] F. I. Diakogiannis, F. Waldner, and P. Caccetta, "Looking for change? roll the dice and demand attention."
- [10] M. Zhang and W. Shi, "A feature difference convolutional neural network-based change detection method," *TGRS*, pp. 1–15, 2020.
- [11] J. Chen, Z. Yuan, J. Peng, L. Chen, H. Huang, J. Zhu, Y. Liu, and H. Li, "Dasnet: Dual attentive fully convolutional siamese networks for change detection in high-resolution satellite images," *IEEE Journal of Selected Topics in Applied Earth Observations and Remote Sensing*, vol. 14, pp. 1194–1206, 2021.
- [12] S. Saha, F. Bovolo, and L. Bruzzone, "Building change detection in vhr sar images via unsupervised deep transcoding," *IEEE Transactions on Geoscience and Remote Sensing*, pp. 1–13, 2020.
- [13] F. Jiang, M. Gong, T. Zhan, and X. Fan, "A semisupervised gan-based multiple change detection framework in multi-spectral images," *IEEE Geosci. Remote. Sens. Lett.*, vol. 17, no. 7, pp. 1223–1227, 2020.
- [14] J. Liu, K. Chen, G. Xu, X. Sun, M. Yan, W. Diao, and H. Han, "Convolutional neural network-based transfer learning for optical aerial images change detection," vol. 17, pp. 127–131, 2020.
- [15] D. Wang, J. Zhang, B. Du, G.-S. Xia, and D. Tao, "An Empirical Study of Remote Sensing Pretraining," *arXiv:2204.02825 [cs]*, Apr. 2022.
- [16] O. Manas, A. Lacoste, X. G. i Nieto, D. Vazquez, and P. Rodriguez, "Seasonal contrast: Unsupervised pre-training from uncurated remote sensing data," in *2021 IEEE/CVF International Conference on Computer Vision (ICCV)*. Los Alamitos, CA, USA: IEEE Computer Society, oct 2021, pp. 9394–9403. [Online]. Available: <https://doi.ieeecomputersociety.org/10.1109/ICCV48922.2021.00928>
- [17] M. Leenstra, D. Marcos, F. Bovolo, and D. Tuia, "Self-supervised pre-training enhances change detection in sentinel-2 imagery," *Part of the Lecture Notes in Computer Science book series (LNCS, volume 12667)*, 2021, Jan. 2021.
- [18] P. Akiva, M. Purri, and M. Leotta, "Self-Supervised Material and Texture Representation Learning for Remote Sensing Tasks," *CoRR*, Dec. 2021, arXiv: 2112.01715. [Online]. Available: <http://arxiv.org/abs/2112.01715>
- [19] E. Sanchez, M. Serrurier, and M. Ortner, "Learning disentangled representations of satellite image time series," *CoRR*, Mar. 2019.
- [20] K. He, H. Fan, Y. Wu, S. Xie, and R. Girshick, "Momentum contrast for unsupervised visual representation learning," in *2020 IEEE/CVF Conference on Computer Vision and Pattern Recognition (CVPR)*, 2020, pp. 9726–9735.
- [21] X. Chen and K. He, "Exploring simple siamese representation learning," *CoRR*, vol. abs/2011.10566, 2020. [Online]. Available: <https://arxiv.org/abs/2011.10566>
- [22] K. Ayush, B. Uzket, C. Meng, K. Tanmay, M. Burke, D. Lobell, and S. Ermon, "Geography-aware self-supervised learning," *ICCV*, 2021.
- [23] C. Tao, J. Qia, G. Zhang, Q. Zhu, W. Lu, and H. Li, "TOV: The Original Vision Model for Optical Remote Sensing Image Understanding via Self-supervised Learning," *arXiv:2204.04716 [cs]*, Apr. 2022.
- [24] J. Kang, R. Fernandez-Beltran, P. Duan, S. Liu, and A. J. Plaza, "Deep Unsupervised Embedding for Remotely Sensed Images Based on Spatially Augmented Momentum Contrast," *IEEE Transactions on Geoscience and Remote Sensing*, vol. 59, no. 3, pp. 2598–2610, Mar. 2021.
- [25] V. Stojnic and V. Risojevic, "Self-supervised learning of remote sensing scene representations using contrastive multiview coding," in *Proceedings of the IEEE/CVF Conference on Computer Vision and Pattern Recognition (CVPR) Workshops*, June 2021.
- [26] A. M. Swope, X. H. Rudelis, and K. T. Story, "Representation learning for remote sensing: An unsupervised sensor fusion approach," Aug. 2021.
- [27] H. Jung, Y. Oh, S. Jeong, C. Lee, and T. Jeon, "Contrastive Self-Supervised Learning With Smoothed Representation for Remote Sensing," *IEEE Geoscience and Remote Sensing Letters*, pp. 1–5, 2021.
- [28] C. Agastya, S. Ghebremusse, I. Anderson, C. Reed, H. Vahabi, and A. Todeschini, "Self-supervised contrastive learning for irrigation detection in satellite imagery," *CoRR*, vol. abs/2108.05484, 2021. [Online]. Available: <https://arxiv.org/abs/2108.05484>
- [29] K. Cha, J. Seo, and Y. Choi, "Contrastive multiview coding with electro-optics for SAR semantic segmentation," *CoRR*, vol. abs/2109.00120, 2021. [Online]. Available: <https://arxiv.org/abs/2109.00120>
- [30] W. Li, H. Chen, and Z. Shi, "Semantic segmentation of remote sensing images with self-supervised multitask representation learning," *IEEE Journal of Selected Topics in Applied Earth Observations and Remote Sensing*, vol. 14, pp. 6438–6450, 2021.
- [31] H. Li, Y. Li, G. Zhang, R. Liu, H. Huang, Q. Zhu, and C. Tao, "Global and Local Contrastive Self-Supervised Learning for Semantic Segmentation of HR Remote Sensing Images," *IEEE Transactions on Geoscience and Remote Sensing*, vol. 60, pp. 1–14, 2022.

- [32] M. Tarasiou and S. Zafeiriou, "Embedding Earth: Self-supervised contrastive pre-training for dense land cover classification," *arXiv:2203.06041 [cs]*, Mar. 2022.
- [33] W. Li, K. Chen, H. Chen, and Z. Shi, "Geographical knowledge-driven representation learning for remote sensing images," *IEEE Transactions on Geoscience and Remote Sensing*, vol. 60, pp. 1–16, 2022.
- [34] E. Maggiori, Y. Tarabalka, G. Charpiat, and P. Alliez, "Can semantic labeling methods generalize to any city? the inria aerial image labeling benchmark," in *2017 IEEE International Geoscience and Remote Sensing Symposium, IGARSS 2017, Fort Worth, TX, USA, July 23-28, 2017*. IEEE, 2017, pp. 3226–3229.
- [35] S. Ji, S. Wei, and M. Lu, "Fully convolutional networks for multisource building extraction from an open aerial and satellite imagery data set," *IEEE Trans. Geoscience and Remote Sensing*, vol. 57, no. 1, pp. 574–586, 2019.
- [36] D. Peng, L. Bruzzone, Y. Zhang, H. Guan, H. Ding, and X. Huang, "Semicdnet: A semisupervised convolutional neural network for change detection in high resolution remote-sensing images," *IEEE Transactions on Geoscience and Remote Sensing*, pp. 1–16, 2020.
- [37] C. Zhang, P. Yue, D. Tapete, L. Jiang, B. Shangguan, L. Huang, and G. Liu, "A deeply supervised image fusion network for change detection in high resolution bi-temporal remote sensing images," *ISPRS*, vol. 166, pp. 183–200, 2020.
- [38] H. Chen, W. Li, and Z. Shi, "Adversarial instance augmentation for building change detection in remote sensing images," *IEEE Transactions on Geoscience and Remote Sensing*, pp. 1–16, 2021.
- [39] X. Zhang, W. Yu, and M.-O. Pun, "Multilevel deformable attention-aggregated networks for change detection in bitemporal remote sensing imagery," *IEEE Transactions on Geoscience and Remote Sensing*, vol. 60, pp. 1–18, 2022.
- [40] Q. Shi, M. Liu, S. Li, X. Liu, F. Wang, and L. Zhang, "A Deeply Supervised Attention Metric-Based Network and an Open Aerial Image Dataset for Remote Sensing Change Detection," *IEEE Trans. Geosci. Remote Sens.*, vol. 60, pp. 1–16, Jun. 2021.
- [41] T. Liu, M. Gong, D. Lu, Q. Zhang, H. Zheng, F. Jiang, and M. Zhang, "Building Change Detection for VHR Remote Sensing Images via Local-Global Pyramid Network and Cross-Task Transfer Learning Strategy," *IEEE Trans. Geosci. Remote Sens.*, vol. 60, pp. 1–17, Nov. 2021.
- [42] Z. Li, C. Yan, Y. Sun, and Q. Xin, "A densely attentive refinement network for change detection based on very-high-resolution bitemporal remote sensing images," *IEEE Transactions on Geoscience and Remote Sensing*, vol. 60, pp. 1–18, 2022.
- [43] T. Lei, J. Wang, H. Ning, X. Wang, D. Xue, Q. Wang, and A. K. Nandi, "Difference Enhancement and Spatial-Spectral Nonlocal Network for Change Detection in VHR Remote Sensing Images," *IEEE Trans. Geosci. Remote Sens.*, vol. 60, pp. 1–13, Dec. 2021.
- [44] S. Hafner, Y. Ban, and A. Nascetti, "Urban Change Detection Using a Dual-Task Siamese Network and Semi-Supervised Learning," *arXiv*, Apr. 2022.
- [45] W. G. C. Bandara and V. M. Patel, "Revisiting Consistency Regularization for Semi-supervised Change Detection in Remote Sensing Images," *arXiv:2204.08454 [cs, eess]*, Apr. 2022.
- [46] V. Ruzicka, S. D'Aronco, J. D. Wegner, and K. Schindler, "Deep active learning in remote sensing for data efficient change detection," in *Proceedings of MACLEAN: MACHINE Learning for EARTH ObservatioN Workshop co-located with the European Conference on Machine Learning and Principles and Practice of Knowledge Discovery in Databases (ECML/PKDD 2020), Virtual Conference, September 14-18, 2020*, ser. CEUR Workshop Proceedings, T. Corpetti, D. Ienco, R. Interdonato, M. Pham, and S. Lefèvre, Eds., vol. 2766. CEUR-WS.org, 2020. [Online]. Available: <http://ceur-ws.org/Vol-2766/paper2.pdf>
- [47] X. Wang, P. Du, D. Chen, S. Liu, W. Zhang, and E. Li, "Change detection based on low-level to high-level features integration with limited samples," vol. 13, pp. 6260–6276, 2020.
- [48] J. Li, X. Huang, and X. Chang, "A label-noise robust active learning sample collection method for multi-temporal urban land-cover classification and change analysis," *ISPRS Journal of Photogrammetry and Remote Sensing*, vol. 163, pp. 1–17, may 2020.
- [49] H. Sahbi, S. Deschamps, and A. Stoian, "Active learning for interactive satellite image change detection," *arXiv*, Oct. 2021.
- [50] M. Neumann, A. S. Pinto, X. Zhai, and N. Houlsby, "Training general representations for remote sensing using in-domain knowledge."
- [51] V. Risojevic and V. Stojnic, "The Role of Pre-Training in High-Resolution Remote Sensing Scene Classification," *arXiv:2111.03690 [cs]*, Nov. 2021, *arXiv: 2111.03690*. [Online]. Available: <http://arxiv.org/abs/2111.03690>
- [52] W. Li, K. Chen, H. Chen, and Z. Shi, "Geographical Knowledge-Driven Representation Learning for Remote Sensing Images," *IEEE Trans. Geosci. Remote Sens.*, vol. 60, pp. 1–16, Oct. 2021.
- [53] H. Chen, Y. Zao, L. Liu, S. Chen, and Z. Shi, "Semantic decoupled representation learning for remote sensing image change detection," *arXiv*, Jan. 2022.
- [54] X. Liu, F. Zhang, Z. Hou, Z. Wang, L. Mian, J. Zhang, and J. Tang, "Self-supervised learning: Generative or contrastive."
- [55] T. Chen, S. Kornblith, M. Norouzi, and G. E. Hinton, "A simple framework for contrastive learning of visual representations," in *Proceedings of the 37th International Conference on Machine Learning, ICML 2020, 13-18 July 2020, Virtual Event*, ser. Proceedings of Machine Learning Research, vol. 119. PMLR, 2020, pp. 1597–1607. [Online]. Available: <http://proceedings.mlr.press/v119/chen20j.html>
- [56] X. Chen, H. Fan, R. Girshick, and K. He, "Improved baselines with momentum contrastive learning."
- [57] J. Grill, F. Strub, F. Altché, C. Tallec, P. H. Richemond, E. Buchatskaya, C. Doersch, B. Á. Pires, Z. Guo, M. G. Azar, B. Piot, K. Kavukcuoglu, R. Munos, and M. Valko, "Bootstrap your own latent - A new approach to self-supervised learning," in *Advances in Neural Information Processing Systems 33: Annual Conference on Neural Information Processing Systems 2020, NeurIPS 2020, December 6-12, 2020, virtual*, H. Larochelle, M. Ranzato, R. Hadsell, M. Balcan, and H. Lin, Eds., 2020. [Online]. Available: <https://proceedings.neurips.cc/paper/2020/hash/f3ada80d5c4ee70142b17b8192b2958e-Abstract.html>
- [58] X. Wang, R. Zhang, C. Shen, T. Kong, and L. Li, "Dense contrastive learning for self-supervised visual pre-training," in *2021 IEEE/CVF Conference on Computer Vision and Pattern Recognition (CVPR)*, 2021, pp. 3023–3032.
- [59] Z. Wu, Y. Xiong, S. X. Yu, and D. Lin, "Unsupervised feature learning via non-parametric instance discrimination," in *2018 IEEE/CVF Conference on Computer Vision and Pattern Recognition (CVPR)*. Los Alamitos, CA, USA: IEEE Computer Society, jun 2018, pp. 3733–3742. [Online]. Available: <https://doi.ieeecomputersociety.org/10.1109/CVPR.2018.00393>
- [60] N. Jean, S. Wang, A. Samar, G. Azzari, D. B. Lobell, and S. Ermon, "Tile2vec: Unsupervised representation learning for spatially distributed data," in *The Thirty-Third AAAI Conference on Artificial Intelligence, AAAI 2019, The Thirty-First Innovative Applications of Artificial Intelligence Conference, IAAI 2019, The Ninth AAAI Symposium on Educational Advances in Artificial Intelligence, EAAI 2019, Honolulu, Hawaii, USA, January 27 - February 1, 2019*. AAAI Press, 2019, pp. 3967–3974.
- [61] C. Tao, J. Qi, W. Lu, H. Wang, and H. Li, "Remote Sensing Image Scene Classification With Self-Supervised Paradigm Un-

- der Limited Labeled Samples,” *IEEE Geoscience and Remote Sensing Letters*, pp. 1–5, 2020.
- [62] B. Peng, Q. Huang, and J. Rao, “Spatiotemporal contrastive representation learning for building damage classification,” in *IEEE International Geoscience and Remote Sensing Symposium, IGARSS 2021, Brussels, Belgium, July 11-16, 2021*. IEEE, 2021, pp. 8562–8565.
 - [63] P. Jain, B. Schoen-Phelan, and R. Ross, “Self-Supervised Learning for Invariant Representations from Multi-Spectral and SAR Images,” *arXiv*, May 2022.
 - [64] Y. Chen and L. Bruzzone, “Self-supervised change detection in multiview remote sensing images,” *IEEE Transactions on Geoscience and Remote Sensing*, vol. 60, pp. 1–12, 2022.
 - [65] S. Saha, P. Ebel, and X. X. Zhu, “Self-supervised multisensor change detection,” *IEEE Transactions on Geoscience and Remote Sensing*, vol. 60, pp. 1–10, 2022.
 - [66] Y. Chen and L. Bruzzone, “Self-supervised Remote Sensing Images Change Detection at Pixel-level,” *arXiv*, May 2021.
 - [67] X. Huang and S. Belongie, “Arbitrary style transfer in real-time with adaptive instance normalization.”
 - [68] K. He, X. Zhang, S. Ren, and J. Sun, “Deep residual learning for image recognition,” in *2016 IEEE Conference on Computer Vision and Pattern Recognition, CVPR 2016, Las Vegas, NV, USA, June 27-30, 2016*. IEEE Computer Society, 2016, pp. 770–778.
 - [69] T.-Y. Lin, P. Dollár, R. Girshick, K. He, B. Hariharan, and S. Belongie, “Feature Pyramid Networks for Object Detection,” in *2017 IEEE Conference on Computer Vision and Pattern Recognition (CVPR)*. IEEE, Jul. 2017, pp. 936–944.
 - [70] L. Chen, G. Papandreou, I. Kokkinos, K. Murphy, and A. L. Yuille, “Deeplab: Semantic image segmentation with deep convolutional nets, atrous convolution, and fully connected crfs,” *IEEE Trans. Pattern Anal. Mach. Intell.*, vol. 40, no. 4, pp. 834–848, 2018.
 - [71] Y. Tian, D. Krishnan, and P. Isola, “Contrastive multiview coding,” in *Computer Vision – ECCV 2020: 16th European Conference, Glasgow, UK, August 23–28, 2020, Proceedings, Part XI*. Berlin, Heidelberg: Springer-Verlag, 2020, p. 776–794. [Online]. Available: https://doi.org/10.1007/978-3-030-58621-8_45
 - [72] H. Wang, Z. Wang, M. Du, F. Yang, Z. Zhang, S. Ding, P. Mardziel, and X. Hu, “Score-cam: Score-weighted visual explanations for convolutional neural networks,” in *2020 IEEE/CVF Conference on Computer Vision and Pattern Recognition Workshops (CVPRW)*. Los Alamitos, CA, USA: IEEE Computer Society, jun 2020, pp. 111–119. [Online]. Available: <https://doi.ieeecomputersociety.org/10.1109/CVPRW50498.2020.00020>